RSC Advances

Cite this: *RSC Advances*, 2012, **2**, 4759–4767

www.rsc.org/advances

PAPER

Preparation of dendritic NiFe films by electrodeposition for oxygen evolution

Kyung Ho Kim, Jin You Zheng, Woonsup Shin* and Young Soo Kang*

Received 10th February 2012, Accepted 10th March 2012
DOI: 10.1039/c2ra20241g

Dendritic materials are attractive as catalysts due to their highly ordered structure and high surface area. Herein, we report a NiFe dendritic nanostructure obtained by a simple electrodeposition without template. The control of concentration, potential, and pH plays an important role in the formation of the dendritic nanostructures. The longer and thinner NiFe dendritic nanostructure was obtained by changing the potential from −1.1 to −1.3 V *vs.* Ag/AgCl and a highly ordered nanostructure was obtained at the low pH of 2. NiFe dendritic material obtained at a potential of −1.3 V in pH 2.00 at 0.025 M $NiSO_4$ and 0.025 M $FeSO_4$ has a three-dimensional nanostructure. The growth mechanism of the NiFe dendritic nanostructure was investigated by SEM and the ED pattern of TEM. EDS, XRD, and XPS were used to investigate elemental composition, crystalline structure, and the chemical state of the as-obtained NiFe dendritic material. The efficiency of water-oxidation catalysts is critically influenced by the surface conditions and controlling the surface state is a major factor in developing an artificial photosynthetic system which stores the sunlight energy by water-splitting and carbon dioxide reduction in aqueous solution. Hence, we tested the NiFe dendritic nanomaterial as an oxygen-evolving catalyst and found that it shows oxygen evolution at 0.44 V *vs.* Ag/AgCl in 1 M NaOH solution.

1. Introduction

Fundamental properties of materials generally depend on size, shape, and composition. Nanosized materials have attracted the attention of researchers due to size-dependent effects on the properties, such as catalytic, electrochemical, mechanical, magnetic, and optical properties.[1] Highly ordered nanoscale materials with different structures, such as wire-like,[2,3] tube-like,[4] flower-like,[5,6] and dendrite-like,[7] owing to high surface area and structural advantages, were synthesized for their various applications, such as gas sensors,[8] dye-sensitized solar cells,[9] lithium ion batteries,[10,11] and photocatalysts.[12] As an advanced strategy in size and shape-controlled materials, dendritic nanomaterials have been a focus of interest because of chemical and physical properties, and have been investigated for their potential applications, such as a methanol oxidation catalyst[13] as well as nitrate[14] and glucose sensors.[15]

Formation of these dendritic materials was controlled by surface energy under non-equilibrium conditions.[16,17] When the system is under non-equilibrium states, overpotential plays a key role in formation of dendrites. Dendritic structures are not interfered with charge transfer by grain boundaries due to physically connected networks which are composed of center-branches and side-branches or leaves.[18] Therefore dendritic nanomaterials show new possibilities for better catalysts.

Korea Center of Artificial Photosynthesis, Department of Chemistry, Sogang University, Seoul 121-742, South Korea.
E-mail: yskang@sogang.ac.kr (Y. S. Kang); shinws@ sogang.ac.kr (W. Shin)

Another important factor determining properties of materials is the chemical composition. NiFe alloy materials have been used not only as memory and storage devices[19,20] but also catalysts for the oxygen evolution reaction (OER)[21] and hydrogen evolution reaction[22] because of their mechanical, chemical, and magnetic properties.[23,24] Different NiFe structures, such as nanoparticles,[25] nanowires,[26,27] nanorods,[28] nanotubes,[29] and flower-like structures[30] were synthesized by various techniques, but synthesis of the dendritic NiFe structure has not yet been reported.

Compared to other techniques, electrochemical technique is a very attractive method due to deposition rate control by potentials or currents, thicknesses control of films by deposition time, selectivity of deposition parts on a substrate, and low cost of equipments. Furthermore, electrodeposition is a suitable method for study on synthesis and mechanism of dendritic material because growth rate and mass transport rate is controlled by concentrations of salts and applied potentials.[18] Recently, so many dendritic metals and metal alloys obtained by electrodeposition have been reported, such as Fe,[31] Co,[32] Ni,[33] Cu,[14] Zn,[18] Pd,[34] Ag,[35] Pt,[36] Au,[37] AgCu,[38] CuNi,[15] NiPb[39] and so on. In addition, highly ordered NiFe nanowires,[26,27] nanorods and nanotubes[29] have been fabricated by template-assisted electrodeposition. However, the template-based synthesis is difficult and complicated. Herein, we easily and conveniently synthesized well-ordered NiFe dendritic nanostructures by templateless electrodeposition.

Dendritic materials have so far been fabricated by researchers, but their applications have rarely been studied. The NiFe alloys have been known as materials for OER in the previous

reports.[40,41] Nickel oxide electrodes containing iron impurities showed low oxygen overpotential in basic solution.[42] Potvin and Brossard[43] insisted that a 45/55% nickel-iron alloy had the lowest oxygen overvoltage for OER in basic solution at 80 °C and McFarland *et al.*[44] discussed that NiFe-oxide films electrodeposited on hematite substrates played a great role as a catalyst for OER. Herein, we electrochemically tested the dendritic NiFe films as catalysts for OER in artificial photosynthesis that store sunlight energy by water-splitting in aqueous solution. Research of oxygen-evolving catalysts is important because oxygen evolution overpotential decrease the conversion efficiency of light to current in water-oxidation reaction.[45] Dendritic NiFe films as a catalyst are expected to increase the catalytic efficiency in electrochemical water-oxidation reaction due to high surface area and efficient electron transfer.

In this research, we discussed electrochemical synthesis of dendritic NiFe films and the effects of factors in different deposition conditions, such as the concentration of precursor, potentials, pH, and electrolytes. Detailed characterizations for morphologies, structures, and mechanism of as-prepared NiFe films are investigated. Catalytic activity for OER was also studied in the as-obtained samples by using the cyclic voltammetric technique.

2. Experimental section

2.1 Preparation of dendritic NiFe materials

The synthesis of NiFe dendritic materials was performed in a three-electrode system by using a potentiostat (CHI 900) instrument. High-purity Ni foil (Aldrich, 99.98%, 0.5 mm thick) was used as the working electrode, which is placed at the bottom of the electrochemical cell. The area of Ni foil for NiFe electrodeposition was fixed to be 0.2 cm^2 by O-ring size. Ni foil was polished by sand paper, and cleaned by acetone (Jin Chemical, 99+%) and deionized water (> 18 MΩ, Nanopure Ultrapure water system). A Pt wire was used as the counter electrode, Ag/AgCl (saturated in 3 M KCl) as the reference electrode.

NiFe dendrites were prepared on the Ni foil by electrolytic deposition in a solution containing 0.025 M $NiSO_4$ (Yakuri Pure Chemicals, 98.5+%), 0.025 M $FeSO_4$ (Junsei Chemical, 98.5+%) and 0.1 M Na_2SO_4 (Jin Chemical, 99+%) at room temperature. A small amount of 1 M H_2SO_4 (Jin Chemical, 95+%) was added to the mixed solution to adjust the pH. The mixed solution containing 0.025 M $NiCl_2$ (Duksan Pure Chemical, 96+%), 0.025 M $FeCl_2$ (Sigma-Aldrich, 99%) and 0.1 M NaCl (Samchun Pure Chemical, 99%) was used to confirm how an electrolyte affects the formation of dendrites.

Electrolytic deposition was carried out under constant potentials of −1.1, −1.2, and −1.3 V in the mixed solution at pH 3.0, 2.5, and 2.0 for 300 s to investigate the effect of potentials and pHs and also under constant potentials of −1.3 V at pH 2.0 for 300 s with mixed solutions containing 0.010, 0.025, and 0.050 M precursor ions to check morphologic characterization by various concentrations. In addition, the electrochemical deposition was carried out under a constant potential of −1.3 V in the mixed solution at pH 2.0 for 30 s, 50 s, 100 s, and 900 s in order to study a growth mechanism of the NiFe dendritic structure. The different solution containing 0.025 M $NiCl_2$ (Duksan Pure Chemical, 96+%), 0.025 M $FeCl_2$ (Sigma-Aldrich, 99%) and 0.1 M NaCl (Samchun Pure Chemical, 99%) was used to confirm how an electrolyte affects the formation of dendrites. After an electrochemical deposition, the electrodes were washed with deionized water and kept in a petri dish at room temperature.

2.2 Characterization

The morphology and crystal structure of the obtained electrodes by electrodeposition at the different pH, potentials, and concentrations were characterized by field-emission scanning electron microscope (FE-SEM, JEOL JSM-6700F), and high-resolution transmission electron microscope (HR-TEM, JEOL JEM-2010). The investigation of FE-SEM was carried out at a voltage of 13 kV with a spot size of 40 nm at room temperature. The analysis of HR-TEM was carried out at an accelerating voltage of 200 kV with Cu grids as substrates. Energy-dispersive X-ray spectroscopy (EDX, Oxford Instruments, INCA x-sight) was used to analyse the elemental composition in the electrodeposited material. X-ray diffraction (XRD, PHILIPS X'Pert-MPD System, the X-ray is Cu-Kα radiation with λ = 0.154056 nm) was used to check the crystal structure of the as-obtained material. To prevent the substrate influence for XRD analysis, the deposits were taken off from the Ni electrode by the tape. The XPS spectra for the dendritic NiFe were acquired using a Thermo VG Scientific Multilab 2000 system equipped with the Mg KR X-ray source at 1253.60 eV to analyze chemical oxidation and binding state. Its binding energy was referenced to the C1s line at 285.12 eV.

2.3 Electrochemical measurement of oxygen evolution reaction (OER) by dendritic NiFe film

The electrocatalytic property of the OER was measured by a cyclic voltammetry technique using the three-electrode system (the as-prepared NiFe working electrode, the Pt wire counter electrode, and the Ag/AgCl reference electrode). The dendritic NiFe film and the electroplating NiFe film as the working electrode were electrodeposited at −1.3 V in pH 2.0 with different salt concentrations of 0.025 M and 0.050 M. The working electrodes were rinsed with deionized water and 1 M NaOH (Jin Chemical, 95+%) solution before using. The cyclic voltammetric experiments were performed in 1 M NaOH solution at room temperature.

2.4 Bulk electrolysis

Bulk electrolysis was carried out in a stirred solution at room temperature by using the potentiostat. The as-obtained NiFe dendritic film as the working electrode was completely immersed in 2 mL of 1 M NaOH solution. A homemade Ag/AgCl (sat. KCl) electrode used as counter and reference electrodes was positioned in the vicinity of a catalyst film. The charge profile was obtained by bulk electrolysis at 0.50 V *vs.* Ag/AgCl in 1 M NaOH solution at pH 14.

3. Results and discussion

3.1 Formation and characterization of dendritic NiFe nanostructure

The films were prepared by electrochemical reduction of Ni^{2+} and Fe^{2+} ions in aqueous solution. The standard reduction

potentials of Ni^{2+}/Ni and Fe^{2+}/Fe are −0.433 V and −0.637 V *vs.* Ag/AgCl (saturated in 3 M KCl), respectively. Therefore codeposition of nickel–iron was conducted at more negative potentials than the potential of −0.637 V. Fig. 1 shows FE-SEM images of the films electrodeposited at −1.3 V in pH 2.0 with an aqueous solution containing 0.025 M $NiSO_4$ and 0.025 M $FeSO_4$ as metal sources and 0.1 M Na_2SO_4 as the supporting electrolyte. Dendritic nanostructures were fabricated at all regions of the film, as shown in a low magnification image. A high magnification image shows that three-dimensional (3D) dendritic nanostructures are formed on the film.

The characterizations of dendritic films were analyzed by different equipments of EDX, XRD, TEM, and XPS. Energy Dispersive X-ray spectra (EDX) in Fig. 2 were obtained from the region marked in the FE-SEM image of the prepared film. The sample was prepared under conditions stated in Fig. 1 with a different deposition time of 900 s. These spectra correspond to Ni, Fe, and O, as shown in Fig. 2. The EDX analysis consistently indicates that the ratio of Ni/Fe (40.39/45.32) is close to 1 in Table 1.

Elemental composition of the dendritic NiFe in a center-branched spot was shown in Fig. 3. The ratio of Ni to Fe given in Table 2 was approximately 1 as the same result not only at a center-branch but also at a side-branch of the dendritic material. But the atomic ratio of O measured from each spot was different according to the parts exposed to air or not.

The crystalline structure of the dendritic NiFe film was investigated by XRD in Fig. 4. The upper and lower lines given in Fig. 4 indicate XRD patterns of the Ni plate and the as-prepared sample, respectively. The positions of all diffraction peaks corresponding to (111), (200), (220), and (311) planes at the lower line indicate that the as-obtained film is corresponding with NiFe alloy which consists of face-centered cubic structure indexed in JCPDS.

The TEM image and ED pattern of the dendritic NiFe film are presented in Fig. 5. The TEM image shows well-defined dendritic nanostructures in the as-obtained NiFe film and the ED pattern shows the crystal orientation in which dendritic NiFe nanostructures grow. Leaves of dendrites attached at the center-branch of dendritic NiFe material grow in the direction of the (220) plane. We confirmed that different leaves of the dendritic NiFe nanostructure grew to the regular (220) direction.

The surface of the electrodeposited NiFe dendritic film was investigated by X-ray photoelectron spectroscopy (XPS) in Fig. 6. The dendritic NiFe nanomaterial was prepared on a copper electrode to avoid the influence of Ni. All elemental

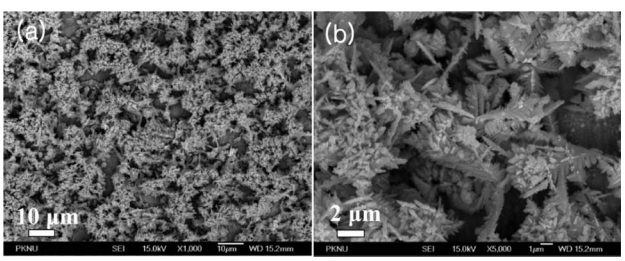

Fig. 1 FE-SEM images of dendritic NiFe structures in different magnifications of (a) and (b) obtained at −1.3 V in pH 2.0 for a deposition time of 300 s.

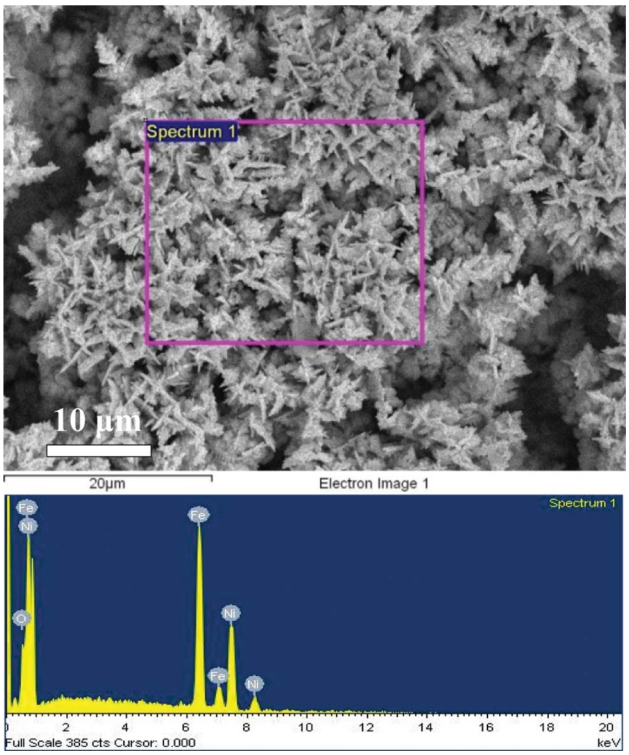

Fig. 2 The FE-SEM and EDX image of dendritic NiFe nanostructures obtained at −1.3 V in pH 2.0 for a deposition time of 900 s.

Table 1 Weight and atomic percentages of elemental composition of the dendritic NiFe film by EDX analysis

Element	Weight (%)	Atomic (%)
O K	4.45	14.29
Fe K	49.33	45.32
Ni K	46.21	40.39
Totals	100.00	100.00

peaks obtained from the dendritic NiFe film are shown in Fig. 6 (a). The XPS profiles of Ni $2p^3/_2$, Fe $2p^3/_2$, and O 1s show chemical states of Ni and Fe on the surface. Ni $2p^3/_2$ peaks at 852.7, 856.5 eV according to chemical states indicates that it is composed of metallic Ni, and $Ni(OH)_2$ or NiO.[37] In the Fe $2p^3/_2$ spectrum, three peaks at 707.0, 709.2, and 711.8 eV are related to metallic Fe, $Fe(OH)_2$ or FeO, and FeO(OH), respectively.[46] It is difficult to distinguish metal hydroxide and metal oxide in the XPS spectrum because both of them have similar binding energies. The main peak at 531.5 eV in the O spectrum indicates oxygen bound to Ni^{2+} and Fe^{3+}, and the other peak at 529.6 eV belongs to oxygen bound to Fe^{2+}.[46] According to XPS data on the NiFe surface in Table 3, the elemental composition of the dendritic NiFe film corresponds to the result by EDX analysis except for high oxygen ratio. In anomalous codeposition, reduction of Fe^{2+}/Fe could be faster than reduction of Ni^{2+}/Ni for very short electrodeposition time due to the high rate constant (k) of an iron reduction. With increasing deposition time, reduction rates of Ni^{2+} and Fe^{2+} ions became almost the same by diffusion.[47] Therefore the ratio of Ni/Fe is close to 1.

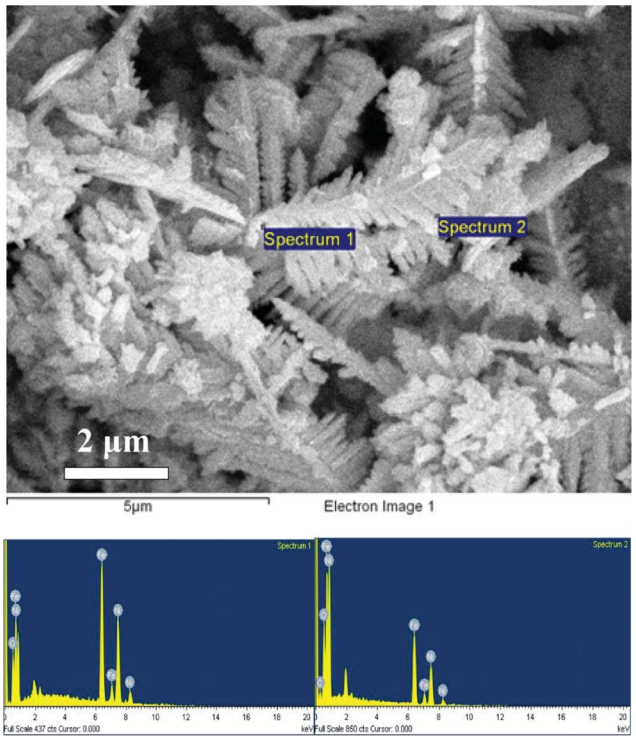

Fig. 3 The FE-SEM image of dendritic NiFe nanostructures obtained at −1.3 V in pH 2.0 for a deposition time of 300 s and EDX images at different spots.

Table 2 Weight and atomic percentages of elemental composition of the dendritic NiFe film at different spots by EDX analysis

Spectrum 1		Spectrum 2	
Element	Atomic (%)	Element	Atomic (%)
O K	15.77	**O K**	38.43
Fe K	41.50	**Fe K**	31.35
Ni K	42.73	**Ni K**	30.22
Totals	100.00	**Totals**	100.00

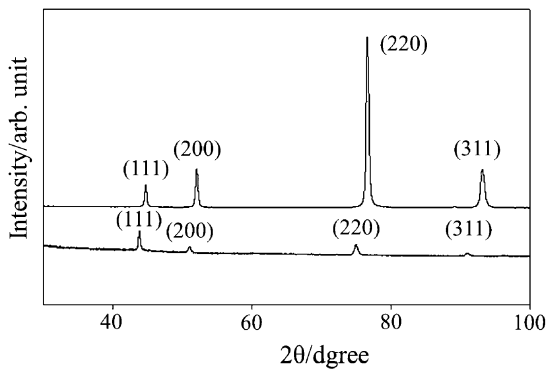

Fig. 4 XRD patterns of the plated Ni electrode (upper line) and the dendritic NiFe film (lower line) obtained at −1.3 V in pH 2.0 for a deposition time of 300 s.

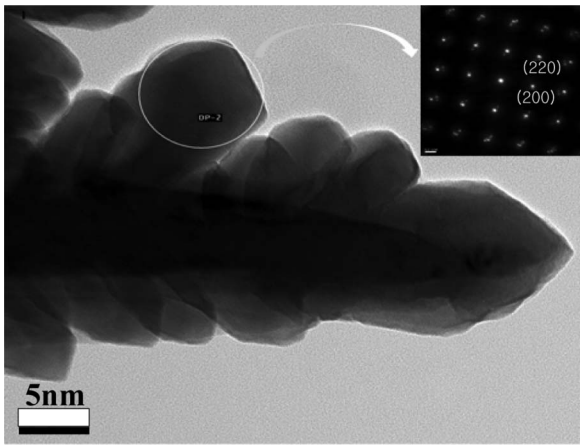

Fig. 5 The TEM and ED pattern of the dendritic NiFe nanostructure obtained at −1.3 V in pH 2.0 for a deposition time of 300 s.

3.2 Mechanism of dendritic growth

To study the mechanism of NiFe dendritic growth, the dendritic films of NiFe alloys were electrodeposited at −1.3 V at pH 2 for different deposition times of 30 s, 50 s, 100 s, and 900 s and their FE-SEM images are given in Fig. 7.

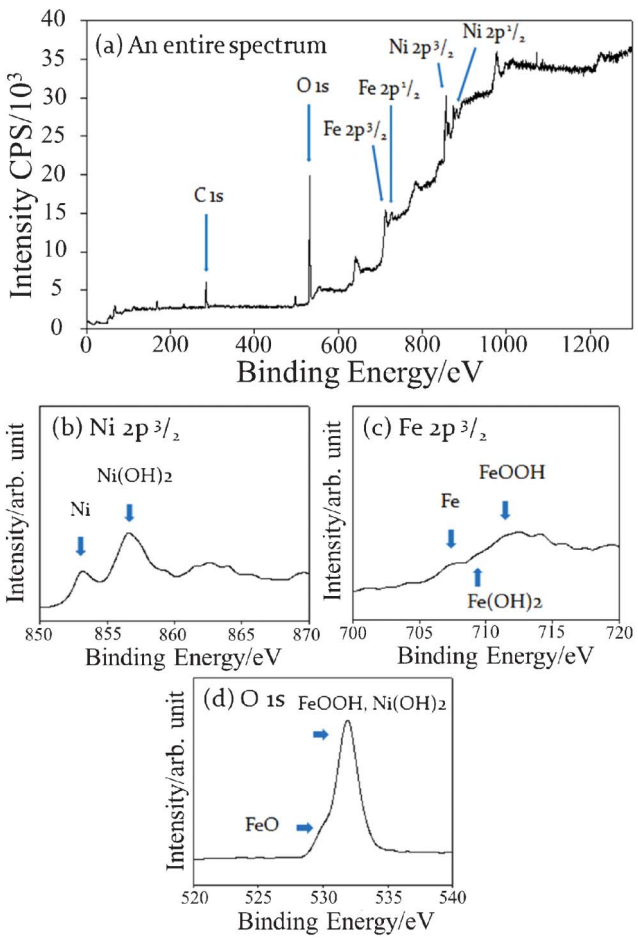

Fig. 6 XPS spectra of dendritic NiFe materials before Ar ion sputtering: (a) an entire XPS spectrum, (b) a Ni $2p^3/_2$ spectrum, (c) a Fe $2p^3/_2$ spectrum, (d) an O 1s spectrum.

Table 3 Atomic percentage and peak binding energy of chemical composition on the surface of the dendritic NiFe film by XPS analysis

Name of Peaks	Peak BE (eV)	Atomic (%)
O 1s	531.89	65.78
Fe $2p^3/_2$	711.93	17.33
Ni $2p^3/_2$	856.65	16.89

Nucleation of NiFe materials occurred on the substrate by the reduction of metal ions during a deposition time of 30 s. The nuclei of NiFe alloy are distributed in all regions on the substrate and are smaller than 1 μm in length in Fig. 7 (a). These nuclei grow to motif crystals composed of single crystals with a hexagonal pattern. Well-defined hexagonal crystals are connected to another one, which is a characteristic structure of the dendritic materials. The dendritic crystals grow along a (220) plane of the fixed direction as confirmed by the ED pattern of TEM. Herein, it is assumed that other planes, except for the (220) plane, are adsorbed by anions in order to decrease surface energy. Therefore these crystals grow along a (220) plane with relatively high surface energy and are form stem-like structures of the center branches.

Growth of side-branched crystals in the stem-like structure would be controlled by adsorption of anions and the limitation of mass transport on the facets of hexagonal crystals. All side-branched crystals also grow in the (220) plane due to the difference of the surface energy by anion effects. Detailed shapes of side-branches as shown in the TEM image depend on the difference of mass transport by positions of the hexagonal facets. While reduction of metal ions proceeds, edges of the hexagonal crystal grow faster than regions such as the plane surfaces due to a high concentration of metal ions by diffusion. As a result, side-branched crystals are formed to hexagonal patterned crystals and grow further as stem-like crystals. FE-SEM images in Fig. 7 show that crystals gradually grow to dendritic structures.

3.3 Effects of concentrations of precursors, potentials, pHs, and kinds of electrolytes on dendritic formation

FE-SEM images of NiFe films in Fig. 8 show different morphologies on different concentration of precursors. Samples were prepared in the conditions given in Fig. 1 with different concentrations of 0.01–0.05 M $NiSO_4$ and 0.01–0.05 M $FeSO_4$. In Fig. 8 (a), non-dendritic structures were observed in the NiFe film, which was electrodeposited at low concentration of 0.01 M $NiSO_4$ and 0.01 M $FeSO_4$, owing to the slow growth rate of crystals and diffusion rate of metal ions. Slow crystal growth is caused by the low concentration of precursor ions, where metal sources are not sufficiently supplied. The mass transport also has a critical parameter on slow crystal growth by the limitation of diffusion at the interface between the substrate and bulk solution. Therefore, crystalline structures are rounded shapes in order to minimize the surface energy. The NiFe film deposited at the concentration of 0.025 M metallic salts was consisted of well-regulated dendritic structures by suitable control of growth rate and diffusion rate. The electroplated NiFe film was prepared at a high concentration of metallic salts, as shown in Fig. 8 (c). Numerous crystals formed at high concentration grow sufficiently fast by an increase of the mass transport rate, leading to an electroplated surface.

The effect of potential on the formation of dendritic NiFe nanostructures was discussed from the results in Fig. 9. These films shown in Fig. 9 were prepared by the reduction of Ni^{2+} and Fe^{2+} ions at different deposition potentials. The reduction potential of Ni^{2+} and Fe^{2+} measured by using a Ag/AgCl (sat') reference electrode is experimentally −0.8 and −1.1 V, respectively. To obtain NiFe alloy, the deposition potential was applied at over or equal to −1.1 V.

Three different crystal growth patterns were shown in the NiFe films electrodeposited at −1.1, −1.2, and −1.3 V. When a deposition potential of −1.1 V was applied, NiFe nanoparticles were formed on the substrate. The crystals grow slowly at low

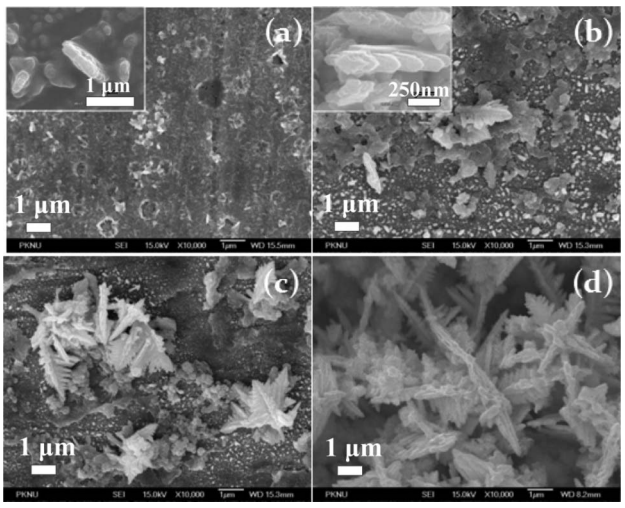

Fig. 7 FE-SEM images of dendritic NiFe nanostructures obtained at −1.3 V at pH 2.0 for different deposition times; (a) 30 s, (b) 50 s, (c) 100 s, and (d) 900 s. Insets show different magnifications.

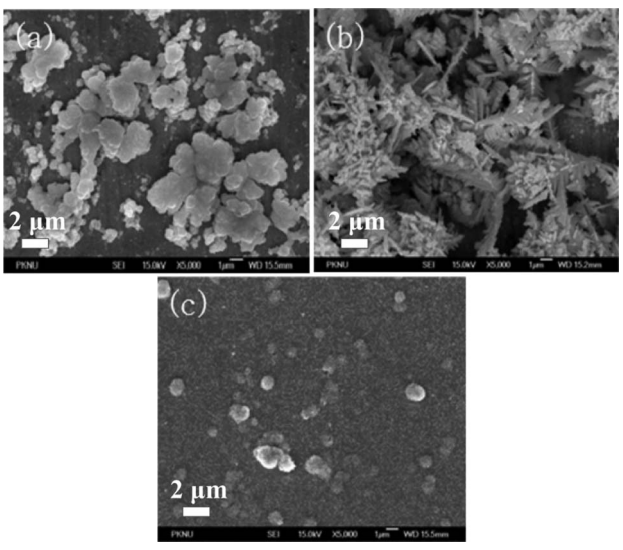

Fig. 8 FE-SEM images of NiFe film structures obtained at −1.3 V at pH 2.0 for a deposition time of 300 s at different concentrations; (a) 0.01 M, (b) 0.025 M, and (c) 0.050 M $NiSO_4$, $FeSO_4$, respectively.

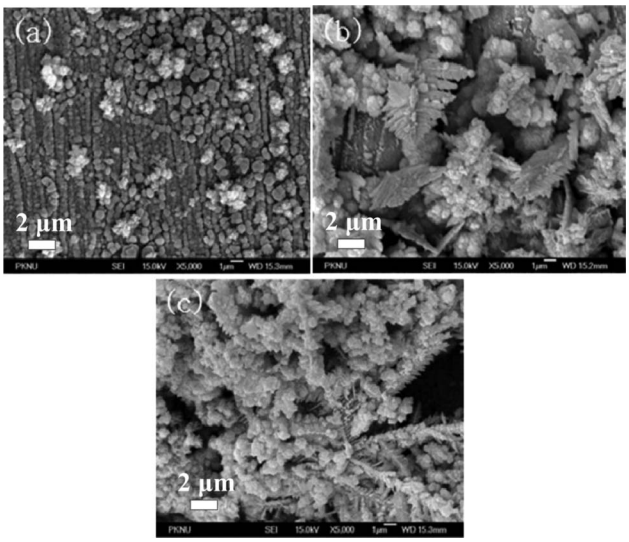

Fig. 9 FE-SEM images of NiFe structures obtained at pH 3.0 for a deposition time of 300 s at different potentials; (a) −1.1, (b) −1.2, and (c) −1.3 V.

potential because crystal growth by the reduction of metal ions is affected by reduction rate. Crystalline structures under these conditions consisted of rounded shapes, not hexagonal shapes, in order to form energetically stable crystals on the surface. Different NiFe dendritic structures were observed in Fig. 9 (b) and (c) when more negative potentials were applied. Overpotential at −1.2 V allowed the dendritic structure to form in a non-equilibrium state, as shown in Fig. 9 (b). Excessive energy above activation energy level can be obtained by overpotential and is needed to form a dendritic structure. Because the reduction rate of metal ions on the substrate is faster than the mass transport rate of metal ions from bulk solution to the surface, nuclei grow to hexagonal motif crystals. Therefore the potential plays a key role in the formation of dendritic structures. Fast crystal growth by the overpotential on the surface generates hexagonal-patterned crystals, and then the hexagonal crystal grows to a dendritic structure by the diffusion of metal ions.

The dendritic NiFe structures formed by increasing overpotential at −1.3 V in Fig. 9 (c) became thinner and longer than the dendritic structure obtained at a low overpotential of −1.2 V. As overpotentials were increased, a lot of nuclei could be produced at a fixed concentration so the dendritic structure grows to be long and thin in a high nucleation density. On the other hand, the dendrites fabricated under low overpotential conditions were thick and short by relatively slow crystal growth rate and low nucleation density. We conclude that the thickness and the length of dendrites can be controlled by overpotentials applied on the substrate.

Non-dendritic materials given in Fig. 10 were consisted of nickel–iron hydroxide on the basis of the expected results in Table 4. Elemental analysis of two distinctive morphologies in the NiFe film was conducted by using EDX. One part of a silky flower-like material consisted of nickel–iron hydroxide due to the relatively higher atomic ratio of oxygen/metals (69.98/27.41) given in Table 4. Hydrogen evolution at the negative potentials ($2H_2O + 2e^- \rightarrow H_2 + 2OH^-$, $E^\circ = -1.025$ V *vs.* Ag/AgCl) results in high pH by generation of hydroxide ions on the surface, which

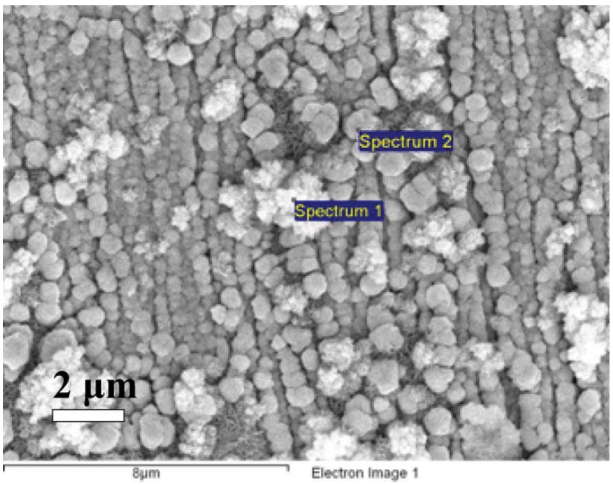

Fig. 10 FE-SEM images of the NiFe film obtained at −1.1 V in pH 3.0 for a deposition time of 300 s.

Table 4 Atomic percentages of elemental composition of the NiFe film at different spots by EDX analysis

Spectrum 1		Spectrum 1	
Element	Atomic (%)	Element	Atomic (%)
O K	69.98	**O K**	28.84
Fe K	15.20	**Fe K**	37.56
Ni K	12.21	**Ni K**	33.60
S K	2.61	**Totals**	100.00
Totals	100.00		

causes formation of nickel–iron hydroxides. Another spot of a dendritic material is composed of metallic nickel–iron due to relatively low atomic ratio of oxygen/metals (28.84/71.16). Oxygen from the EDX spectrum can be detected by the exposure in the air. Therefore we expect that the control of pH is important because hydroxide ions have effect on formation of the dendritic structure.

The effect of pH on the dendritic NiFe structure was investigated at a pH of 2.0, 2.5, and 3.0 in the same potential. Different morphologies of the NiFe films fabricated from each pH are shown in Fig. 11. When pH was decreased from 3 to 2, nickel–iron hydroxides were also decreased, resulting in the formation of well-defined dendritic structures. The formation of different morphologies in different pH was influenced by overpotential and hydrogen ion concentration. Thinner and longer dendritic structures were shown in Fig. 11 because higher overpotential with increasing pH was applied to the system. High overpotential increases the hydroxide ion concentration by the reduction of water and has a negative effect on the formation of highly ordered dendritic structures.

Hydrogen ion concentration as another factor affecting the formation of well-defined structures controls the amount of nickel–iron hydroxide by diffusion of hydrogen ions. When the metal and the hydrogen ions approach to the electrode surface by diffusion, these ions compete for the decrease of hydroxide ions with production of the nickel–iron hydroxide or H_2O. The nickel–iron hydroxide is difficult to deposit because H_2O is vigorously produced by the faster diffusion rate of the hydrogen

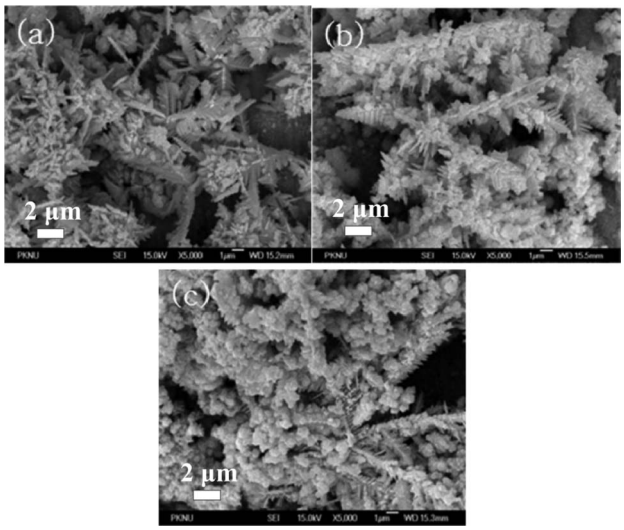

Fig. 11 FE-SEM images of dendritic NiFe structures obtained at −1.3 V for a deposition time of 300 s with different pHs; (a) 2.0, (b) 2.5, and (c) 3.0.

ion than the nickel–iron hydroxide. Therefore the pH control plays a key role in the formation of highly ordered dendritic structures.

The NiFe films were prepared by electrodeposition in the same conditions using only different electrolytes and their morphologies are displayed in Fig. 12. In palladium dendritic nanowires, dendritic structures were synthesized by using sulfate ions but were not fabricated by using chloride ions.[48] However, dendritic structures were observed in all NiFe films prepared by using sulfate and chloride ions as electrolytes. Therefore, kinds of electrolytes have no critical effect on the formation of the NiFe dendritic structures.

3.4 Oxygen evolution reaction (OER) by the dendritic NiFe film

The cyclic voltammetric experiments at the Ni electrode and the as-electrodeposited NiFe film were conducted in 1 M NaOH solution at room temperature in a potential range from −1.1 to 0.6 V at 5 mV s^{-1} (Fig. 13). Both peaks shown a_1 and a_2 correspond to the conversion of nickel(II)–iron(II) hydroxide or oxide to nickel(III)–iron(III) oxy-hydroxide as shown in the following equations. M indicates the NiFe.

$$M(OH)_4 + 2OH^- \leftrightarrow M(O(OH))_2 + 2H_2O + 2e^-$$

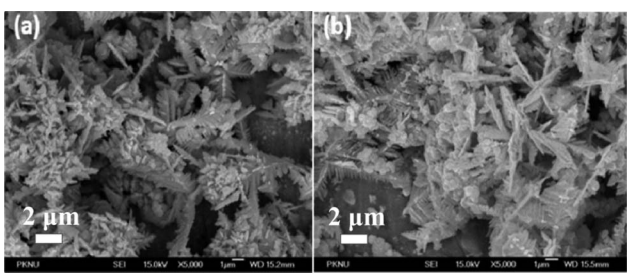

Fig. 12 FE-SEM images of dendritic NiFe structures obtained at −1.3 V in pH 2.0 for a deposition time of 300 s with different electrolytes; (a) sulfate ions and (b) chloride ions.

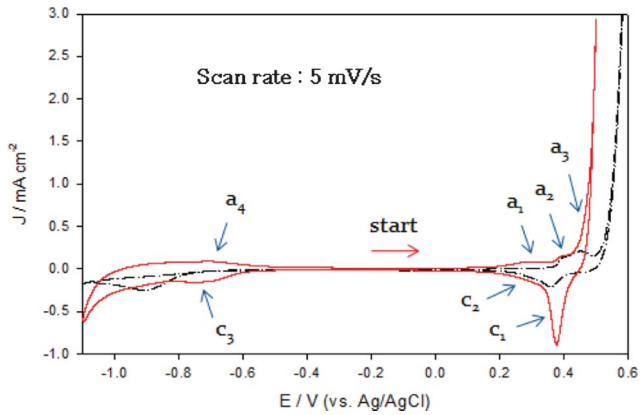

Fig. 13 Cyclic voltammogram in 1.0 M NaOH solution at 298 K at (a) the Ni electrode (dashed and dotted line) and (b) the dendritic NiFe film (solid line).

or

$$MO_2 + 2OH^- \leftrightarrow M(O(OH))_2 + 2e^- \quad (1)$$

The electrodeposited dendritic NiFe films have different phases similar to the reported nanosized $Ni(OH)_2$ where one anodic peak is separated to two peaks due to the conversion of α-$Ni(OH)_2$ to γ-NiO(OH) and β-$Ni(OH)_2$ to β-NiO(OH).[49] The peak at a_3 is obviously O_2 evolution. Although the anodic peak from the conversion of Ni(III)Fe(III)/Ni(IV)Fe(IV) is not observed due to O_2 evolution, the steep cathodic peak at c_1 is shown by the conversion of Ni(IV)Fe(IV)/Ni(III)Fe(III) as in the following equation.

$$M(O(OH))_2 + 2OH^- \leftrightarrow MO_4 + 2H_2O + 2e^- \quad (2)$$

The reduction peak c_2 is responsible for reverse reaction of (1).[49,50] The Ni(III)Fe(III) converts to Ni(II)Fe(II) at this potential. The peak c_3 corresponds to the conversion of Ni(II)Fe(II) to Ni(0)Fe(0) and a_4 corresponds to opposite conversion, as shown in the following equation.[22]

$$M(OH)_4 + 4e^- \leftrightarrow M + 4OH^- \quad (3)$$

The mechanism of the OER in the dendritic NiFe film is shown in Scheme 1. $MO_2(OH)_2$ oxidizes to MO_4 in alkaline solution, and then MO_4 generates oxygen by water-oxidation. At oxygen evolution potential, $M(OH)_4$ is quickly converted to $MO_2(OH)_2$. Therefore the anodic peak of Ni(III)Fe(III)/Ni(IV)Fe(IV) was not observed in the cyclic voltammogram because the oxygen is continuously generated by this cycle. The sharp reduction peak of Ni(IV)Fe(IV)/Ni(III)Fe(III) was shown at a potential of 0.39 V as the evidence of oxidation of Ni(III)Fe(III)/ Ni(IV)Fe(IV).

The cyclic voltammogram for the OER by the dendritic NiFe film, the electroplated NiFe film, and the Ni electrode are shown in Fig. 14. The dendritic NiFe film and the electroplated NiFe film were synthesized under experimental conditions of Fig. 8 (b) and (c). OERs of these electrodes were measured in 1 M NaOH at 5 mV s^{-1} in the potential range 0.1–0.6 V. The dendritic NiFe nanostructure and the electroplated NiFe structure were used to

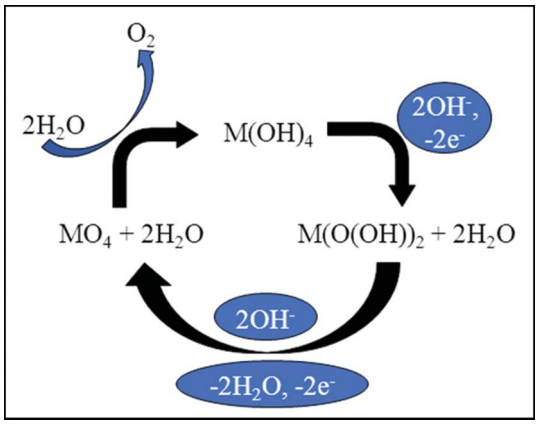

Scheme 1 A schematic diagram of the OER by the NiFe dendritic nanomaterials.

compare the effect of oxygen evolution according to different particle sizes and structures (Fig. 14). The CV of the electroplated NiFe film here is similar to that of electroplating NiFe films already reported.[22] Oxygen evolution on the NiFe alloy occurs at a less positive potential than on the Ni electrode to show that the NiFe alloy has an improved OER activity than the pure Ni.[21] The oxygen evolution potential of the dendritic NiFe film slightly positively shifted compared to that of the electroplated NiFe film. This is because the anodic peak by the conversion of Ni(II)Fe(II)/Ni(III)Fe(III) is shifted to a less positive potential of 0.40 V by different surface area and structures, as shown in Fig. 13. The dendritic NiFe film shows better catalytic activity for the OER due to dendritic properties of high surface area and efficient charge transfer.

3.5 Bulk electrolysis

The charge–time curve was obtained to measure the stability of the dendritic NiFe film and to analyze the amount of O_2 electrochemically produced during bulk electrolysis (Fig. 15). Bulk electrolysis was performed at a fixed potential of 0.50 V *vs.* Ag/AgCl in 1 M NaOH solution using the dendritic NiFe film.

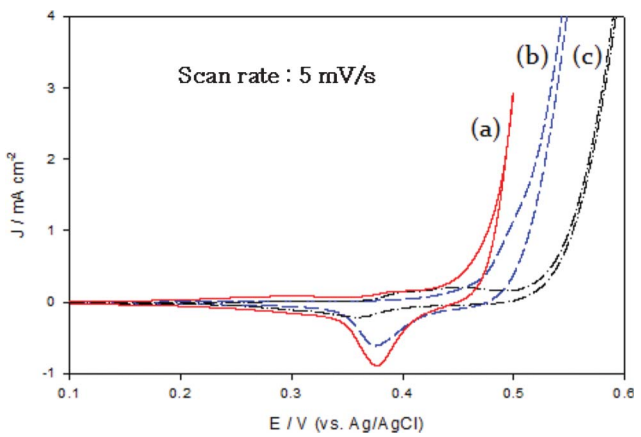

Fig. 14 A cyclic voltammogram in 1 M NaOH solution at 298 K with different electrodes; (a) the electrode modified by dendritic NiFe materials (solid lines), (b) the electrode modified by NiFe plating (dashed line), and (c) the Ni electrode (dashed and dotted line).

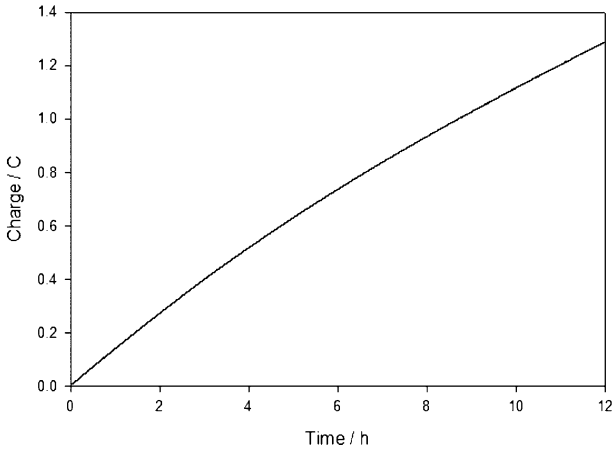

Fig. 15 Accumulated charge *vs.* time profile for bulk electrolysis of the as-prepared NiFe dendritic film at 0.50 V in 1 M NaOH solution at pH 14.0.

The charge consumed increased almost linearly, which indicates that the dendritic NiFe film is stable up to 12 h. Oxygen evolution was observed during bulk electrolysis at 0.50 V but the amount of O_2 was too little to measure directly. Assuming 100% conversion efficiency, the theoretical amount of oxygen produced was calculated by the Faraday's law: $Q = nFN$, where Q is the total charge, n is the number of electrons, F is the Faraday constant, and N is the moles of oxygen. The calculated amounts of oxygen produced after 2 h and 10 h of electrolysis are 0.71 and 2.90 μmol, respectively.

4. Conclusion

The dendritic NiFe film was prepared in the mixed solution containing Ni^{2+} and Fe^{2+} ions without templates by using electrochemical deposition. Well-defined NiFe dendritic crystals were fabricated by selecting electrodeposition conditions, such as electrolyte concentration, potential, pH, and electrolytes. The effect of each factor affecting the formation of the dendritic structures was discussed in this report. Crystal growth rate and mass transport rate play an important role in dendritic formation. In the formation mechanism for the dendritic structure, hexagonal-faceted crystals grow to a stem-like pattern and further grow to 3D dendritic structures by adsorption of anions and high concentration according to the position of well-defined facets. Therefore the developed 3D dendritic NiFe film can achieve remarkable physical properties, such as high surface area and excellent electrochemical properties, such as good charge transfer. The dendritic NiFe film as a catalyst shows outstanding catalytic activity for the OER in alkaline solution due to the merits of the dendritic nanostructures.

Acknowledgements

This work was supported by the Korea Center for Artificial Photosynthesis (KCAP) located in Sogang University funded by the Ministry of Education, Science, and Technology (MEST) through the National Research Foundation of Korea (NRF-2009-C1AAA001-2009-0093879).

References

1 X. L. Xu, J. B. Jia, X. R. Yang and S. J. Dong, *Langmuir*, 2009, **26**, 7627.
2 C. J. Lee, T. J. Lee, S. C. Lyu and Y. Zhang, *Appl. Phys. Lett.*, 2002, **81**, 3648–3650.
3 X. F. Duan and C. M. Lieber, *J. Am. Chem. Soc.*, 2000, **122**, 188–189.
4 Z. F. Ren, Z. P. Huang, J. W. Xu, J. H. Wang, P. Bush, M. P. Siegal and P. N. Provencio, *Science*, 1998, **282**, 1105–1107.
5 H. Zhang, D. R. Yang, X. Y. Ma, Y. J. Ji, J. Xu and D. L. Que, *Nanotechnology*, 2004, **15**, 622.
6 S. Z. Li, H. Zhang, J. Xu and D. R. Yang, *Mater. Lett.*, 2005, **59**, 420.
7 C. D. Gu and T. Y. Zhang, *Langmuir*, 2008, **24**, 12010.
8 Q. Wan, Q. H. Li, Y. J. Chen, T. H. Wang, X. L. He, J. P. Li and C. L. Lin, *Appl. Phys. Lett.*, 2004, **84**, 3654.
9 G. K. Mor, O. K. Varghese, M. Paulose, K. Shankar and C. A. Grimes, *Sol. Energy Mater. Sol. Cells*, 2006, **90**, 2011.
10 M. S. Park, G. X. Wang, Y. M. Kang, D. Wexler, S. X. Dou and H. K. Liu, *Angew. Chem., Int. Ed.*, 2007, **46**, 750.
11 S. Y. Zeng, K. B. Tang, T. W. Li, Z. H. Liang, D. Wang, Y. K. Wang, Y. X. Qi and W. W. Zhou, *J. Phys. Chem. C*, 2008, **112**, 4836.
12 L. S. Zhang, W. Z. Wang, Z. G. Chen, L. Zhou, H. L. Xu and W. J. Zhu, *J. Mater. Chem.*, 2007, **17**, 2526–2532.
13 L. Wang and Y. Yamauchi, *Chem. Mater.*, 2009, **21**, 3562.
14 R. Qiu, H. G. Cha, H. B. Noh, Y. B. Shim, X. L. Zhang, R. Qiao, D. Zhang, Y. I. Kim, U. Pal and Y. S. Kang, *J. Phys. Chem. C*, 2009, **113**, 15891.
15 R. Qiu, X. L. Zhang, R. Qiao, Y. Li, Y. I. Kim and Y. S. Kang, *Chem. Mater.*, 2007, **19**, 4174.
16 T. Kuroda, T. Irisawa and A. Ookawa, *J. Cryst. Growth*, 1977, **42**, 41–46.
17 Y. Oaki and H. Imai, *Cryst. Growth Des.*, 2003, **3**, 711–716.
18 C. M. López and K. S. Choi, *Langmuir*, 2006, **22**, 10625.
19 C. Cheung, G. Palumbo and U. Erb, *Scr. Metall. Mater.*, 1994, **31**, 735.
20 C. Cheung, F. Djuanda, U. Erb and G. Palumbo, *Nanostruct. Mater.*, 1995, **5**, 513.
21 G. Mlynarek, M. Paszkiewicz and A. Radniecka, *J. Appl. Electrochem.*, 1984, **14**, 145–149.
22 R. Solmaz and G. Kardas, *Electrochim. Acta*, 2009, **54**, 3726.
23 A. Afshar, A. G. Dolati and M. Ghorbani, *Mater. Chem. Phys.*, 2002, **77**, 352.
24 A. Sanaty-Zadeh, K. Raeissi and A. Saidi, *J. Alloys Compd.*, 2009, **485**, 402.
25 B. Folch, J. Larionova, Y. Guari, L. Datas and C. Guérin, *J. Mater. Chem.*, 2006, **16**, 4435.
26 C. G. Wu, H. L. Lin and N. L. Shau, *J. Solid State Electrochem.*, 2006, **10**, 198.
27 S. Aravamudhan, K. Luongo, P. Poddar, H. Srikanth and S. Bhansali, *Appl. Phys. A: Mater. Sci. Process.*, 2007, **87**, 773.
28 X. Chu, D. Jiang and C. Zheng, *Sens. Actuat. B*, 2007, **123**, 793.
29 S. Xue, M. Li, Y. Wang and X. Xu, *Thin Solid Films*, 2009, **517**, 5922.
30 T. Xiao, Y. Tang, Z. Jia, D. Li, X. Hu, B. Li and L. Luo, *Nanotechnology*, 2009, **20**, 475603.
31 R. Qiu, J. Y. Zheng, H. G. Cha, M. H. Jung, K. J. Lee and Y. S. Kang, *Nanoscale*, 2012, **4**, 1565.
32 R. Qiu, D. Zhang, P. Wang, X. L. Zhang and Y. S. Kang, *Electrochim. Acta*, 2011, **58**, 699.
33 J. Wang, L. Wei, L. Zhang, Y. Zhang and C. Jiang, *CrystEngComm*, 2012, **14**, 1629.
34 F. Jia, K. Wong and L. Zhang, *J. Phys. Chem. C*, 2009, **113**, 7200.
35 M. V. Mandke, S. Han and H. M. Pathan, *CrystEngComm*, 2012, **14**, 86.
36 J. K. Kawasaki and C. B. Arnold, *Nano Lett.*, 2011, **11**, 781.
37 A. Lahiri, R. Wen, S. Kuimalee, S. Kobayashi and H. Park, *CrystEngComm*, 2012, **14**, 1241.
38 G. M. de Oliveira and I. A. Carlos, *J. Appl. Electrochem.*, 2009, **39**, 1217–1227.
39 C. Z. Yao, Y. X. Tong, H. X. Ma, Q. J. Gong, L. X. Meng, J. H. Yao and D. C. Xia, *J. Electrochem. Soc.*, 2010, **157**, D503.
40 M. D. Thompson and A. L. Kaye, *Trans. Electrochem. Soc.*, 1931, **60**, 229.
41 G. Grube and W. Gaupp, *Ztschr. Electrochem.*, 1939, **45**, 290.
42 D. A. Corrigan, *J. Electrochem. Soc.*, 1987, **134**, 377.
43 E. Potvin and L. Brossard, *Mater. Chem. Phys.*, 1992, **31**, 311.
44 A. Kleiman-Shwarsctein, Y. S. Hu, G. D. Stucky and E. W. McFarland, *Electrochem. Commun.*, 2009, **11**, 1150.
45 M. W. Kanan and D. G. Nocera, *Science*, 2008, **321**, 1072.
46 J. J. Guo, L. Zhang, A. P. Xian and J. K. Shang, *J. Mater. Sci. Technol.*, 2007, **23**, 811.
47 C. Su, F. He, H. Ju, Y. Zhang and E. Wang, *Electrochim. Acta*, 2009, **54**, 6257.
48 Y. J. Song, J. Y. Kim and K. W. Park, *Cryst. Growth Des.*, 2009, **9**, 505–507.
49 H. Zhou and Z. Zhou, *Solid StateIonics*, 2005, **176**, 1909.
50 M. E. G. Lyons and M. P. Brandon, *Phys. Chem. Chem. Phys.*, 2009, **11**, 2203–2217.